

PAPER • OPEN ACCESS

Semi-automatic conformal micro-scale printing with the ultra-precise dispensing (UPD) system

To cite this article: Georg Gramlich *et al* 2025 *Flex. Print. Electron.* **10** 035015

View the [article online](#) for updates and enhancements.

You may also like

- [Exhaled nitric oxide stability over two years in relation to COPD outcomes](#)
Marieann Högman, Christer Janson, Andreas Palm *et al.*
- [Life cycle assessment of an entirely wood floor system designed for carbon negativity, future adaptability, and end-of-life de/re/construction](#)
Muzan Williams Ijeoma, Sovanroth Ou, Amin Nabati *et al.*
- [ICRH modelling of DTT in full power and reduced-field plasma scenarios using full wave codes](#)
A Cardinali, C Castaldo, F Napoli *et al.*



The Electrochemical Society
Advancing solid state & electrochemical science & technology



**249th
ECS Meeting**
May 24-28, 2026
Seattle, WA, US
*Washington State
Convention Center*

Spotlight Your Science

***Submission deadline:
December 5, 2025***

SUBMIT YOUR ABSTRACT

Flexible and Printed Electronics



PAPER

OPEN ACCESS

RECEIVED
3 July 2025

REVISED
11 August 2025

ACCEPTED FOR PUBLICATION
28 August 2025

PUBLISHED
18 September 2025

Original Content from
this work may be used
under the terms of the
[Creative Commons
Attribution 4.0 licence](#).

Any further distribution
of this work must
maintain attribution to
the author(s) and the title
of the work, journal
citation and DOI.



Semi-automatic conformal micro-scale printing with the ultra-precise dispensing (UPD) system

Georg Gramlich^{1,*} , Martin Roemhild² , Jonathan Wendel¹, Lilli Weiss¹, Holger Baur², Uli Lemmer³, Norbert Fruehauf², Thomas Zwick¹ and Akanksha Bhutani¹

¹ Karlsruhe Institute of Technology, Engesserstr. 5, Karlsruhe 76131, Germany

² University of Stuttgart, Allmandring 3b, Stuttgart 70569, Germany

³ Karlsruhe Institute of Technology, Engesserstr. 13, Karlsruhe 76131, Germany

* Author to whom any correspondence should be addressed.

E-mail: georg.gramlich@kit.edu

Keywords: additive manufacturing, printed electronics, UPD printing, conformal printing

Supplementary material for this article is available [online](#)

Abstract

Conformal printing enables the integration of functional structures onto arbitrarily shaped surfaces and therefore has seen a drastic increase in research interest. ultra-precise dispensing (UPD) is a promising technology since it allows to print structures down to 1 μm and thereby pushes the technological limits. However, it typically requires heavy manual intervention for conformal printing, reducing its usefulness and scalability. In this work, we present a semi-automatic approach for conformal printing with the UPD system in which external measurements and subsequent automatic print path generation replace manual scripting and teaching. We compare the printing time and segmentation of three different projection algorithms, and quantify a tolerance window for the alignment. We then introduce the challenge of nozzle drift in long-duration print jobs, which can reach up to 10 s of μm . Additionally, we evaluate three printing approaches in terms of line uniformity and show how it can be improved from 40% increased width at segment junctions to only 7% changes. The developed workflow for conformal printing substantially extends the field of application of UPD printing, and makes it an excellent choice for high-precision conformal printing with structure sizes down to 1 μm .

1. Introduction

In recent years, there has been a significant increase in research on 3D-printed electronics. According to Google Scholar, approximately 16 000 publications containing the term *printed electronics* appeared in the second decade of this century, compared to fewer than 3000 in the first decade. This trend is likely driven by the growing performance and exceptional design flexibility of additively manufactured components.

Printed electronics offer capabilities that are often unattainable through traditional manufacturing techniques. They enable rapid prototyping, offer scalability, and allow mechanically flexible devices [1, 2]. Furthermore, they offer ecological advantages over conventional subtractive-additive

processes such as photolithography or laser ablation. These traditional methods generate substantial material waste and lithography relies on corrosive chemicals, both of which contribute to environmental pollution [3, 4].

In addition to being sustainable, printing technologies enable fast, cost-efficient prototyping, accelerating design cycles and fostering innovation. This versatility has made printed electronics attractive for a wide range of applications. Notable examples include biomedical systems, such as implantable battery-free sensors for hemodynamic monitoring [5] and wearable health diagnostics [6, 7].

Moreover, flexible hybrid electronics combine the mechanical adaptability of printed components with the computational power of conventional silicon-based ICs [8]. These systems promise innovation in

wearables [9], industrial [10], environmental [11], agricultural [12], and structural health monitoring applications [13].

More recently, the topic of *conformal printing* has gained traction among researchers and engineers in the field. Unlike traditional approaches that rely on flat substrates, conformal printing refers to the deposition of functional inks onto arbitrarily shaped surfaces. This enables electronics to be seamlessly integrated into curved or complex geometries [14], expanding the design space for engineers. Curved electronics offer improved spatial adaptability and better integration into natural environments [15]. Demonstrated advantages include enhanced performance in antennas [16], advanced sensors [17], and biomedical applications [18].

The most commonly used technologies for conformal printing are inkjet, electrohydrodynamic (EHD), and aerosol jet (AJ) printing [15]. Inkjet is a mature technology with wide industrial application and a broad range of inks commercially available. However, the minimum feature size is typically restricted to 20–50 μm [19]. EHD overcomes this limitation but requires high electric fields [20] which may damage sensitive substrates such as integrated circuits. AJ printing can go down to 10–20 μm minimum feature size with ink viscosities between 1 and 1000 cP and a high printing speed [21] but suffers from so-called overspray: Small satellite droplets are deposited next to the printed line which can lead to short circuits in small structures [22].

An emerging technology that overcomes the drawbacks of the previously mentioned technologies is ultra-precise dispensing (UPD) by the company XTPL [23]. This direct-write technique extrudes highly viscous metal nanoparticle ink through a glass nozzle with an opening diameter between 1.5 and 20 μm , enabling extremely fine and accurate patterning down to 1 μm features [24]. However, the nozzle must remain in close proximity to the substrate, and the system lacks an automated surface-following mechanism [25]. As a result, conformal printing with UPD requires extensive manual labor for teaching of the surface topography, making it impractical for medium- or large-scale applications.

To address this limitation, we present a semi-automated approach for conformal printing using the UPD system. Our method significantly reduces the need for manual intervention and enables printing on more complex three-dimensional surfaces. It is based on an offline surface measurement onto which printing paths are projected. This approach has successfully been implemented for large-scale direct ink writing (DIW) systems in [26, 27]. Both studies utilize standard dispensing needles with an opening diameter of several hundred micrometers. Our study transfers this approach to a machine

that supports single-digit micrometer scale features for the first time to the best of our knowledge. We thoroughly analyze the challenges that arise in this regime, notably projection precision and narrow alignment tolerance. We elaborate on the projection algorithm, provide a mathematical analysis of the importance of alignment in direct-write conformal printing, and showcase demonstrators produced using our method. Finally, we draw attention to nozzle drift which is an issue idiosyncratic to the utilized printing system, and propose strategies to improve the uniformity of printed lines.

2. Materials and methods

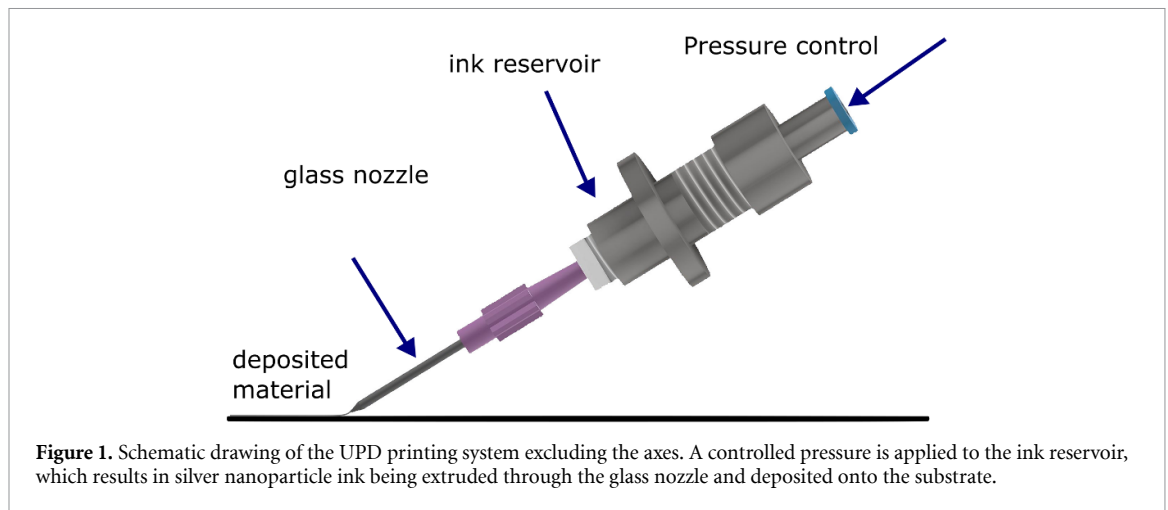
2.1. UPD printing system

The UPD printer by XTPL is a direct-write printing system. It utilizes highly viscous inks that are extruded at pressures of up to 10 bar through a glass nozzle with typical opening diameters of 1.5, 3.5, 5, 8, 10, and 20 μm . Precisely matching the applied pressure to the nozzle geometry and the rheological properties of the used ink enables exceptionally low printing tolerances of 1–2 μm , in the case of CL85 ink, and minimum feature sizes that approximately correspond to the size of the nozzle opening. Figure 1 illustrates the working principle of the UPD printer.

The most commonly used ink in this system is a silver nanoparticle ink provided by XTPL. The ink features an unusually high solid content, giving it shear thinning behavior. This means, it exhibits low viscosity while being extruded and regains high viscosity upon deposition. This rheological behavior enables the formation of printed structures with higher aspect ratios than typically achievable using inkjet or AJ printing.

The nozzle is mounted on a set of precision motion axes, enabling controlled movement in the x , y , and z directions. Both the nozzle motion and the applied pressure can be programmed using a proprietary scripting language. This language supports the use of variables, control loops, and setting motion parameters including direction, velocity, acceleration, and deceleration. It also allows the definition of user-defined functions, which simplifies the implementation of complex functionalities.

One particularly relevant command, which will be discussed further in the context of projection algorithms and line homogeneity, is called *veclineramp*. This command enables the coordinated control of acceleration and deceleration distances in conjunction with printing extrusion pressure and printing speed. It compensates for the inherent delay in pressure buildup and decay at the start and end of a printed line segment. This is especially important in the older versions of the UPD printing system due to limitations of the motion controllers



used in the older systems. Consequently, the nozzle comes to a short rest between printing two adjacent segments, creating bulges if no countermeasures (e.g. veclineramp) are taken.

To ensure continuous material deposition, the nozzle must remain in very close proximity (typically $\leq 1 \mu\text{m}$) to the substrate, or even make physical contact. If this gap is exceeded, the printed lines become interrupted. The nozzle is made from a thin, tapered glass capillary, which is inherently flexible and can deflect by several micrometers without breaking. This allows for an overtravel of approximately $10 \mu\text{m}$ beyond the contact point, increasing the misalignment tolerance. The acceptable overtravel depends on the nozzle and the substrate. However, excessive bending degrades the accuracy of the printed structures and increases the risk of breakage. We therefore recommend limiting the overtravel to less than $3 \mu\text{m}$. This allows the nozzle to passively compensate for substrate height variations of up to $\pm 3 \mu\text{m}$. Larger deviations must be actively incorporated into the programmed toolpath. In this paper, we refer to the nozzle's passive compensation capability as *nozzle slack*.

2.2. 3D printing path creation

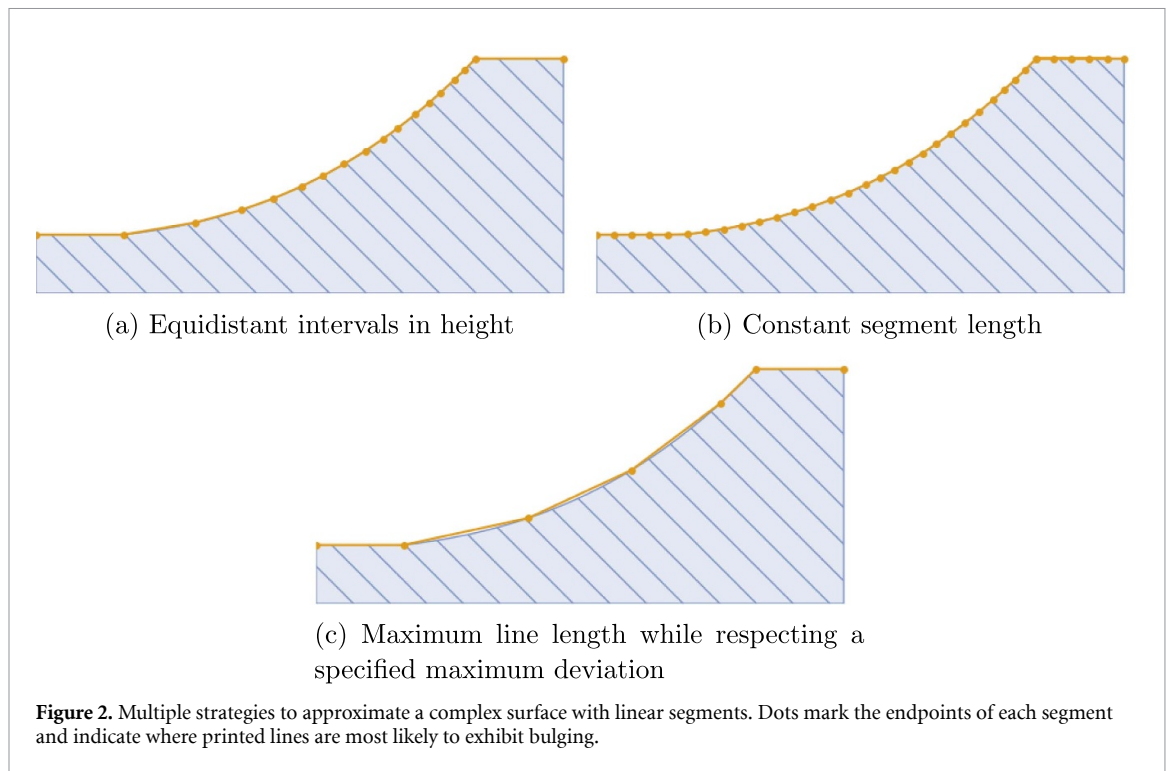
One must choose between two fundamentally different approaches when developing conformal printing for a direct-write system. The first option is to measure the surface height *in situ* and dynamically adapt the printing path during the printing process. This can either be done by measuring the surface geometry before printing—similar to leveling procedures in modern FDM 3D printers—or by continuously sensing the surface in real time during printing. Both approaches require a sensor integrated into the printing system or heavy manual labor if the automatic substrate detection is replaced by manual teaching.

Since our printer does not include such a sensor, and we aimed to develop a versatile approach without complex or costly hardware modifications, we opted for the second strategy: surface measurement outside the printer. For this approach, the surface is scanned in advance, the printing paths are projected onto the measured geometry, and the resulting 3D printing paths are imported into the printer. This method leverages pre-existing surface metrology tools available in many laboratories and avoids the need for additional investment. Its main limitation is that precise alignment is indispensable, as will be discussed in section 3.2. In this work, all surface measurements have been performed with a Bruker Contour GT-K white light interferometer (WLI).

Because the UPD printer can only execute straight-line movements, all curved surfaces must be approximated by sequences of linear segments. Figure 2 shows three strategies for such approximations, each of which will be discussed in terms of their advantages and limitations. All algorithms considered here are assumed to incorporate safeguards against surface edges, which can be achieved through additional checks. The illustrations in figure 2 were generated under the assumption that this additional precautions is in place.

The first approach, shown in figure 2(a), adds a new point whenever the surface height changes by a predefined threshold. This method is intuitive for the UPD system, as it allows the nozzle to incrementally follow the topography only when the built-in nozzle slack is exhausted. However, it produces many short segments, increases printing time, and introduces high variability in segment length depending on local surface steepness. This can lead to inhomogeneous printed lines.

The second strategy, illustrated in figure 2(b), uses line segments of constant length. Compared to the previous method, it offers uniform segment



spacing, simplifying the tuning of printing parameters for optimal line quality. Its drawback is that the fixed segment length must be sufficiently short to approximate the surface accurately. Consequently, most use cases require a short length, which again results in longer printing times.

The third and most sophisticated strategy is shown in figure 2(c). Here, the surface is approximated using the minimal number of segments such that the vertical deviation between the approximation and the actual surface remains below a defined threshold. This keeps the toolpath within the permissible nozzle slack while substantially reducing the number of segments. As a result, many segments become long enough to benefit from the `vecclineramp` command, improving line uniformity. However, some segments may still be too short to allow for pressure and speed ramping, which necessitates additional care to avoid changes in line width.

2.3. Workflow

This section elaborates on our workflow for semi-automatic conformal printing on complex surfaces using the approach described above. Accurate alignment between the measured surface and the physical sample in the printer is essential, as will be discussed in section 3.2. Rotational misalignment around the x - and y -axes can be prevented by leveling both the WLI and the printer to the same reference substrate. In other words, ensuring that both the WLI and the printer are leveled to an identical flat surface guarantees that all features in the measurement data—such

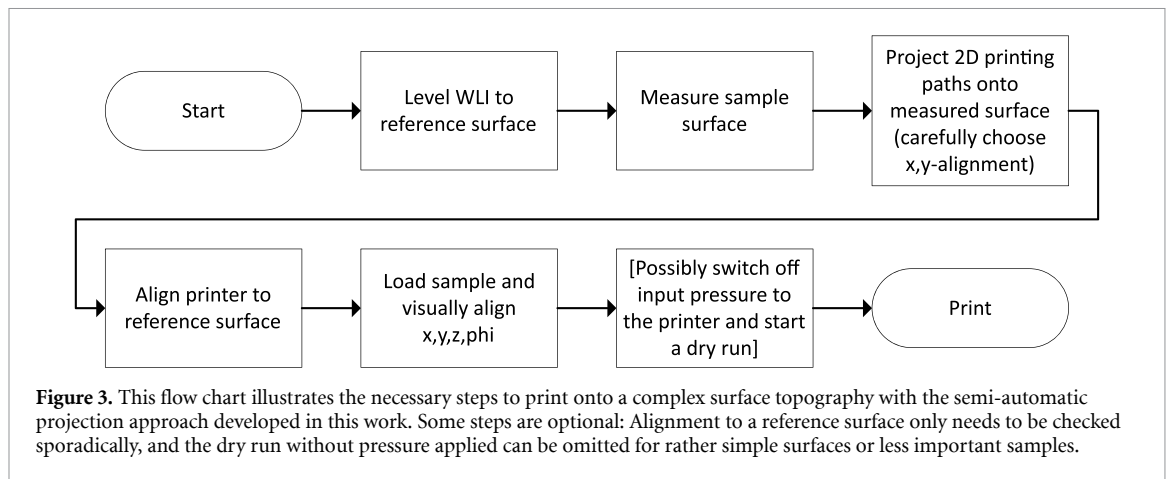
as surface tilt or height steps—are also present on the physical sample. A simple glass slide or silicon wafer serves well as a reference surface.

Once the WLI is leveled, the surface of the actual sample can be measured. If the desired print area exceeds the field of view, x - y stitching can be employed. Because leveling was performed with a physical reference, it is critical to avoid any form of digital leveling or flattening during post-processing of the measurement data.

The resulting surface data must be exported in `.sdf` format, which can be read by the projection software developed in this work. The 2D printing paths are designed in AutoCAD and imported into the projection software as `.dxf` files. It is essential to define the precise location at which the origin of the 2D path (from the `.dxf`) should be positioned on the measured surface. This origin can be determined, for example, using Vision64 in conjunction with Bruker WLI systems. The identified origin must then be manually entered into the projection program.

The software also provides the capability to compensate for rotational misalignment between the imported `.dxf` paths and the measured surface. This is achieved by virtually rotating the surface around the z -axis prior to projection. Once the desired projection algorithm is selected, the 2D paths are projected onto the 3D surface, and a print file suitable for the UPD system can be exported.

Next, the UPD printer must be leveled using the same reference surface that was previously used for leveling the WLI. After leveling, the sample is loaded



and the nozzle is visually aligned to the origin of the print paths. At this point, the print file can be loaded and the printing process initiated.

However, it is prudent to verify the alignment before starting the actual material deposition. To do so, the pressure amplifier can be disabled and any residual pressure in the tubing released. The print job is then started without active pressure, allowing the nozzle to follow the programmed path without depositing ink. This enables visual inspection of the nozzle trajectory across the surface and validation of the alignment.

The complete workflow is summarized in the flow chart shown in figure 3.

3. Results and discussion

3.1. Execution time

The most relevant performance metrics for the projection algorithms described in section 2.2 are: the number of points required to project the printing paths onto the surface, the resulting printing time, and the smoothness (or uniformity) of the printed structures. To evaluate the first two metrics, we created two synthetic surfaces and projected predefined printing paths onto them.

The first surface is a linear ramp with a height of $100\ \mu\text{m}$ and a slope of 45° . The second surface corresponds to the first half of a sine wave with a total length of $200\ \mu\text{m}$ and a peak height of $100\ \mu\text{m}$. Each surface profile is connected to a flat $50\ \mu\text{m}$ -long segment at both ends. The profiles are shown in the second row of table 1. To create surfaces, the profiles were extruded along the x -axis.

The printing paths projected onto these surfaces are five parallel lines spanning from end to end of the profiles. An example of the projected paths on the ramp-shaped surface, as visualized in our projection software, is shown in figure 4. Printing time was measured by executing the generated print scripts on

the printer without attaching a nozzle, thus avoiding ink deposition while preserving realistic timing.

The `vecclineramp` command was used for segments longer than $5\ \mu\text{m}$, with a $10\ \mu\text{m}$ ramp-up and $40\ \mu\text{m}$ ramp-down distance. Segments shorter than or equal to $5\ \mu\text{m}$ were printed without velocity ramping. For the equidistant projection method, a segment length of $5\ \mu\text{m}$ was used, meaning that this method did not utilize the `vecclineramp` command at all. The z -step height and the maximum allowed deviation between the projected path and the original surface were both set to $1\ \mu\text{m}$. Line uniformity was evaluated according to the criteria established in section 3.4.

Table 1 shows that the equidistant height projection method is the least favorable among the three. It results in the longest printing times and the poorest line uniformity. In contrast, the other two methods—constant segment length and maximum segment length—perform similarly in terms of total printing time. The choice between them should be based on the surface topography for each specific application.

If the surface can be approximated using long segments (e.g. segments of $80\ \mu\text{m}$ or more), the maximum segment method yields great uniformity and the shortest printing duration. This is the case for the ramp-shaped surface in table 1. However, when the geometry requires many short segments for accurate approximation—as in the sinusoidal surface—the constant segment method achieves higher uniformity and maintains a comparable or shorter printing time.

3.2. Alignment

In most printing systems, the importance of alignment is well understood. Misalignment typically results in a positional shift of the deposited structure and can lead to functional defects. In conformal printing using the UPD system, however, alignment is even more critical.

If the substrate is shifted, tilted, or rotated relative to the projected 3D print paths, the nozzle may

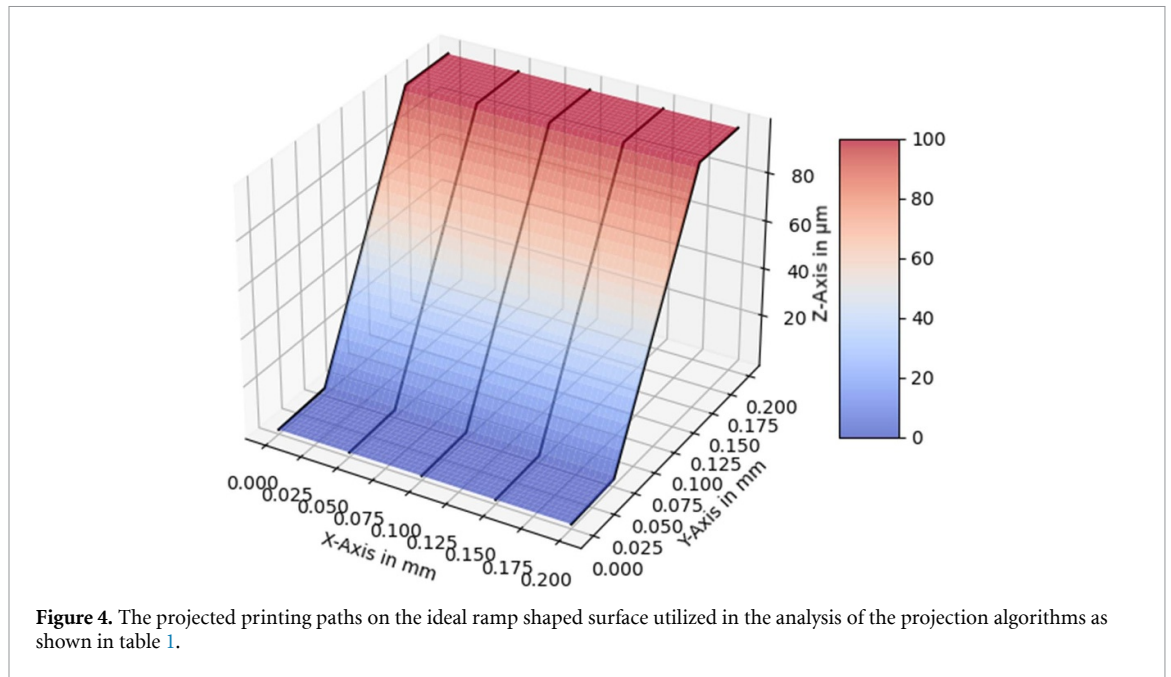






Table 1. Evaluation of the three discussed projection algorithms. Two artificial surface have been used to evaluate the number of points required to map the printing paths to the surface and to measure the printing time. The printing paths consist of five parallel lines spanning from the beginning to the end of the profiles shown in the second line.

Projection method	Number of points		Printing time / s		Uniformity
					
Equidistant height	510	760	197	298	—
Constant segments	245	395	108	174	++
Longest segments	20	350	56	197	+

either crash into the surface or lose contact altogether. In the first case, the nozzle can be damaged due to mechanical stress. In the second case, ink deposition may be interrupted, leading to incomplete or missing structures. Both scenarios produce defective prints and cause process failure.

This section investigates the precision requirements for alignment, depending on the surface geometry to be printed on.

The first key factor is the allowable height deviation along the z -axis. As discussed in section 2.1, the nozzle is made of thin glass and exhibits limited flexibility. The nozzle can be lowered by approximately $10\ \mu\text{m}$ beyond its contact point without breaking. This extra tolerance is referred to as *nozzle slack*. However, excessive bending degrades the accuracy of the printed features and increases the risk of fracture. To reduce this risk, we recommend limiting the overtravel to no more than $3\ \mu\text{m}$. Given that ink deposition remains continuous up to a nozzle-substrate distance of $1\ \mu\text{m}$, a total deviation of up to $\pm 4\ \mu\text{m}$ between the projected path and the actual substrate can be tolerated under these conditions.

Having established the maximum permissible height deviation, we now turn to the types of misalignment that may occur. Broadly, three

misalignment modes are possible: (1) translational shifts along any axis, (2) tilts of the substrate along the x - or y -axes, and (3) in-plane rotation of the substrate around the z -axis. Rotational misalignment around the z -axis can usually be avoided, as the printer stage can be rotated manually, and distinct reference features that support precise rotational alignment can be included into most substrates. Therefore, this section focuses on translational shifts and substrate tilts.

For easier visualization, we consider a ramp-shaped surface along the y -axis, which is constant along the x -axis. It is illustrated in figure 5, where the orange surface corresponds to the measured geometry, and the blue surface represents the actual (misaligned) sample in the printer. The printer will, therefore, follow the orange curve.

Shifting the print paths relative to the actual surface can easily occur if the origin of the print job is not accurately determined. A displacement in the z -direction leads to a direct 1:1 deviation between the programmed path and the actual surface—i.e. every micrometer of z -misalignment results in a micrometer vertical offset. In contrast, shifts in the x - or y -directions interact with surface slope and therefore require a geometric analysis.

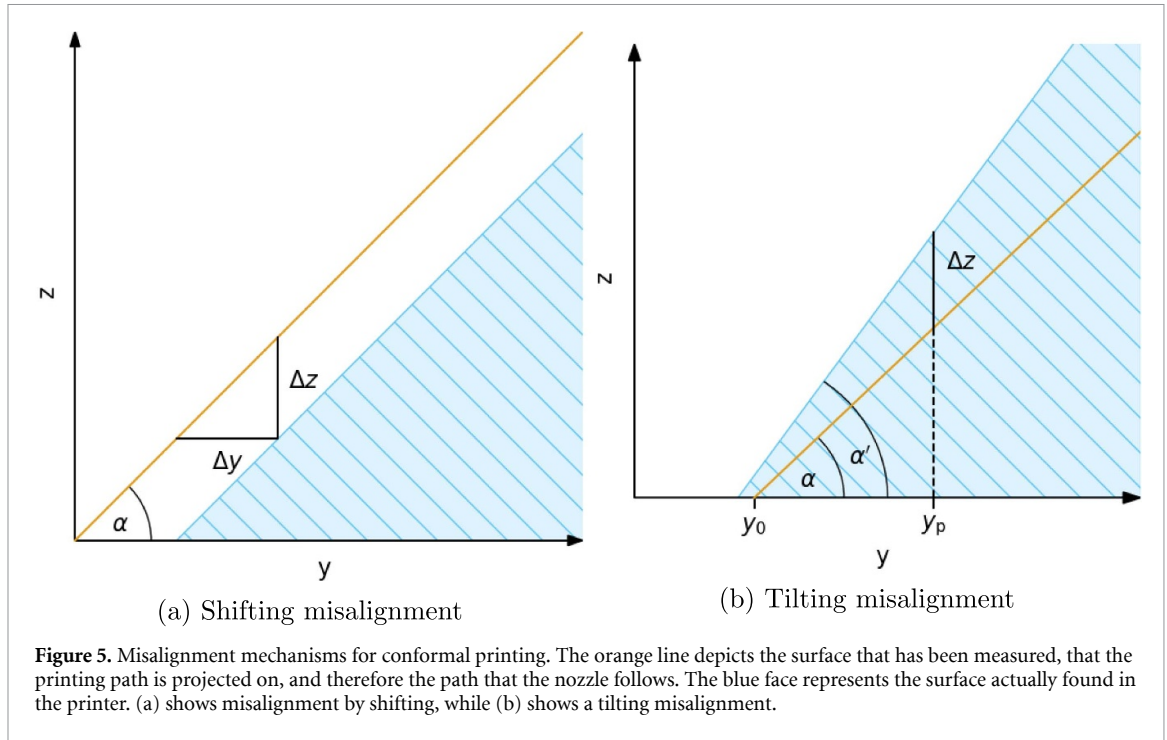


Figure 5(a) shows the effect of a y -directional offset Δy for a surface inclined at an angle α . In this case, the resulting vertical deviation Δz is given by:

$$\Delta z = \Delta y \cdot \tan(\alpha). \quad (1)$$

As expected, a larger positional misalignment results in a greater deviation between the nozzle and the surface. Furthermore, the equation illustrates that this deviation becomes increasingly critical as the surface inclination α grows steeper.

The second type of misalignment worth analyzing is a tilt of the substrate. Figure 5(b) illustrates a ramp surface along the y -axis with an additional tilt around the x -axis. As before, the measured geometry and, therefore, the print paths are shown in orange, while the actual (tilted) substrate surface is depicted in blue.

In the orange curve (measurement data), the slope is assumed to be at zero height ($z = 0$) at position y_0 , and its inclination is α . Due to misalignment, the actual surface is tilted by an additional angle $\Delta\alpha$ around the x -axis, resulting in an effective inclination of $\alpha' = \alpha + \Delta\alpha$. When printing at the location y_p , the vertical displacement between the nozzle and the actual surface is given by

$$\begin{aligned} \Delta z = & y_p \cdot [\tan(\alpha + \Delta\alpha) - \tan(\alpha)] \\ & + y_0 \tan(\alpha) \cdot [1 - \cos(\Delta\alpha) - \tan(\alpha + \Delta\alpha) \\ & \times \sin(\Delta\alpha)]. \end{aligned} \quad (2)$$

Since $\Delta\alpha$ is typically small, a first-order approximation can be used to simplify the expression. This

yields the simplified approximate form:

$$\begin{aligned} \Delta z = & y_p \cdot [\tan(\alpha + \Delta\alpha) - \tan(\alpha)] \\ & - y_0 \Delta\alpha \tan(\alpha) \tan(\alpha + \Delta\alpha). \end{aligned} \quad (3)$$

This simplified form reveals that the resulting z -deviation increases with steeper surface inclinations. It is also amplified at larger distances from the start point of the printjob (y_p) and when the slope is located farther from the origin (y_0).

From practical experience, lateral misalignments in the x - and y -directions can typically be held within $\pm 3 \mu\text{m}$. Given a known surface inclination from the measurement data, equation (1) can be used to estimate the resulting z -deviation from lateral misalignment. This allows one to assess the remaining nozzle slack available to tolerate further deviations. Subsequently, equation (3) can be employed to determine the maximum permissible tilt.

In section 2.3, we introduced a leveling strategy in which both the surface measurement system (e.g. WLI) and the printer are leveled using a common reference plane. By consistently applying this method, we have achieved tilt values ($\Delta\alpha$) too small to detect. This enables reliable printing on steep surfaces, since only translational (shifting) misalignment must be taken into account.

3.3. Nozzle drift

During long print jobs on the UPD printer, nozzle drift can sometimes be observed. This is the phenomenon becomes apparent when the print head is commanded to return to its starting position after

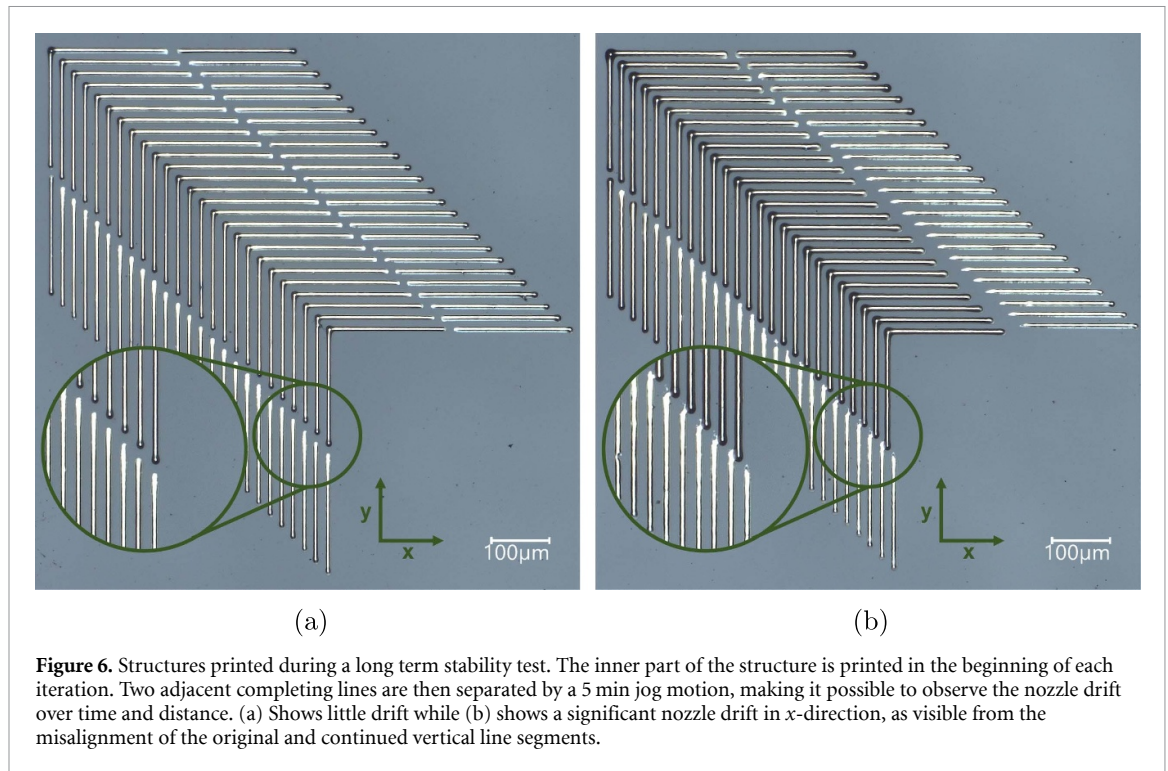


Figure 6. Structures printed during a long term stability test. The inner part of the structure is printed in the beginning of each iteration. Two adjacent completing lines are then separated by a 5 min jog motion, making it possible to observe the nozzle drift over time and distance. (a) Shows little drift while (b) shows a significant nozzle drift in x-direction, as visible from the misalignment of the original and continued vertical line segments.

completing a print job and is found to be misaligned. Nozzle drift can occur along all three spatial axes and directly affects the precision of the printed structures. To systematically analyze this effect, we developed an experimental procedure to quantify nozzle drift.

3.3.1. Experimental setup

The experiment begins by printing a series of equidistant L-shaped alignment patterns. Since these patterns are printed one after another, the drift between them is assumed to be negligible. After completing this initial reference structure, the printer performs a defined jog movement or idles for 5 min. Then, the system extends one L-pattern with one vertical and one horizontal line. This procedure is repeated until all alignment patterns have been extended. Nozzle drift is revealed as a misalignment between the original pattern and the extended segments.

By measuring the offsets between the original and the extended segments, drift in the x - and y -directions can be quantified. Drift in the z -direction is measured directly using the printer's built-in substrate detection function. A structure with minimal drift is shown in figure 6(a), while figure 6(b) shows a case of significant drift along the x -axis.

Each jog/idle cycle lasted 5 min, and a total of 25 alignment structures were printed per test, resulting in approximately 2 h of printing time per test structure. In total, 12 such test structures were fabricated sequentially. Three sequentially fabricated structures always share the same jog/wait pattern.

Including time for printing, performing z -height detection, and rinsing the nozzle for 30 s between patterns, the total duration per test structure was approximately 8 h. The total runtime of the experiment-and hence the duration over which nozzle drift was evaluated-was 32 h and 16 min.

The following jog movement scenarios were investigated:

- (i) A diagonal back-and-forth movement of 50 mm in x and y , and 10 mm in z .
- (ii) The same movement pattern as above, but with all distances scaled by a factor of 0.01.
- (iii) No movement, with an idle wait time of 5 min.
- (iv) A movement pattern simulating the filling of a 100 μm -long pad in the y -direction with lines spaced at a pitch of 3 μm .

Each movement pattern was repeated until a total time of 5 min had elapsed. After each jog sequence, the nozzle was rinsed for 30 s. To capture the precise distance the nozzle moved between patterns, all built-in movement commands (`vecmoveto`, `moveby`, `moveto`) were modified to record the traveled distance. Before extending the alignment structures, the total displacement along each axis and the elapsed time were saved. This procedure enabled a detailed evaluation of nozzle drift as a function of both time and travel distance.

The corresponding print files `3d_userfile_lineramp_nozzle_drift.xtpl` and `nozzle_drift_test.xtpl` are published along this

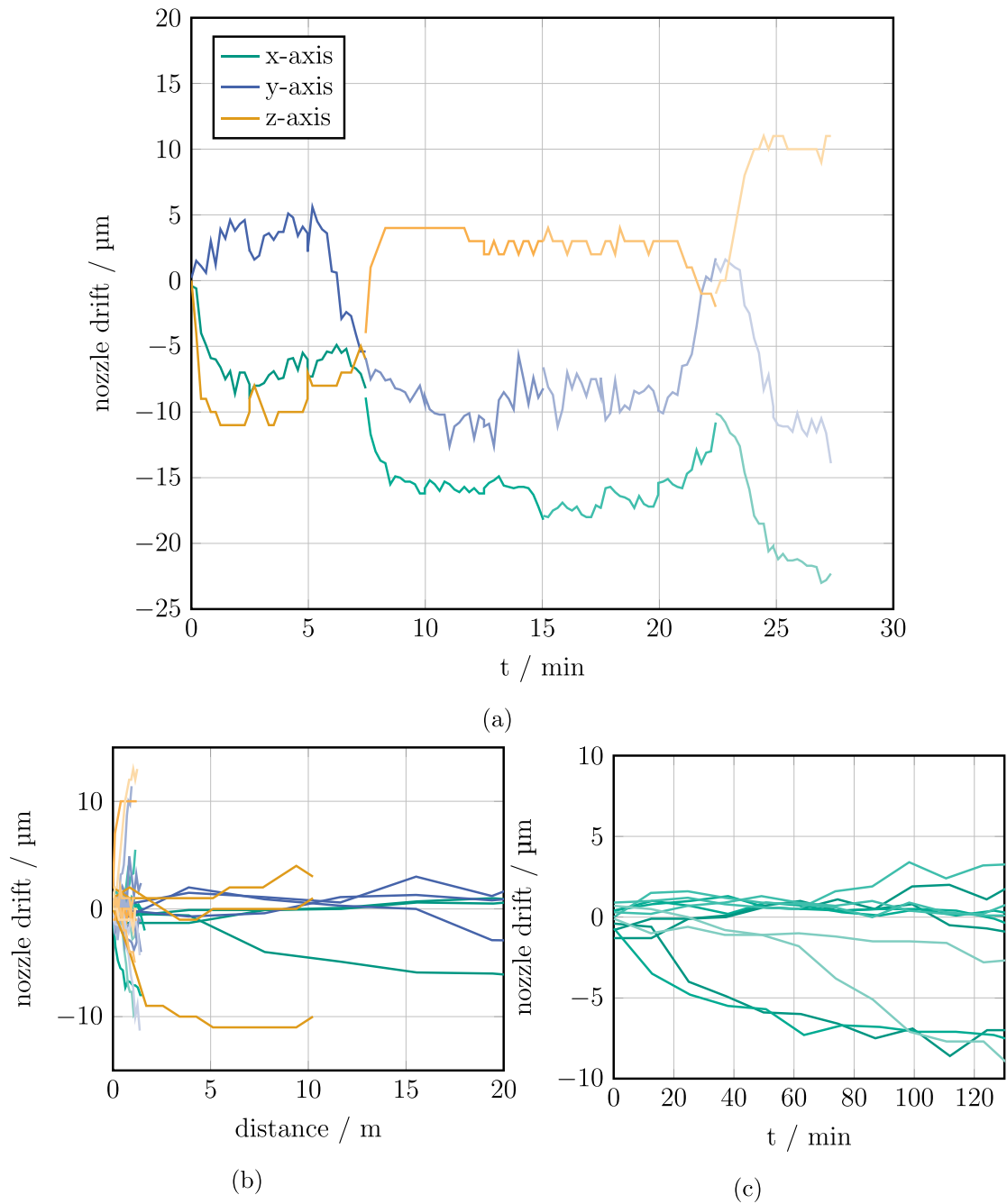


Figure 7. Measured nozzle drift in the UPD printer during a long term test. Jog movements are differentiated by color saturation while axes are color-coded according to the legend in (a). The plots show that nozzle drift is time-dependent rather than distance-dependent, but no pattern with predictive capacity is discernible. (b) and (c) Show the nozzle drift for each of the 12 sequentially printed structures individually, while (a) shows the integrated drift over the entire duration of the experiment.

manuscript. The userfile also contains our custom code used to allow 3d velineramp movements and has to be loaded first. The test can then be started by running main.

An unevenness of the substrate would directly translate into a measurement error of the z-drift. To avoid inaccuracies, we have printed onto a glass slide which was leveled inside the printer effectively removing tilt. The test required a surface of approximately $3.1\text{ mm} \times 4.2\text{ mm}$ over which we measured a maximum surface waviness of $\pm 0.2\text{ }\mu\text{m}$, which is negligible compared to the recorded nozzle drift.

3.3.2. Results and analysis

Figure 7(b) presents nozzle drift as a function of cumulative travel distance along each axis. Each dataset corresponds to one of the 12 test structures. The different jog movement patterns are distinguished by decreasing color saturation, following the same order listed above. The axes are color-coded. The results reveal that reducing movement distance does not reduce nozzle drift; instead, the same amount of drift is compressed into a shorter range. This indicates that nozzle drift is predominantly time-dependent rather than movement-dependent.

This hypothesis is further supported by figure 7(c), which plots x-axis drift as a function of elapsed time. Again, each curve corresponds to one of the 12 structures, using the same color saturation coding. The data suggests that nozzle drift occurs over time, although no clear periodicity or deterministic pattern is observed. Moreover, the type of jog movement does not appear to influence drift behavior.

Figure 7(a) displays the cumulative nozzle drift over the course of the full experiment. Because all 12 structures were printed sequentially, their drift data can be combined to yield a long-term assessment of the process. No correlation is observed between jog movement type (indicated by color saturation) and overall drift. This reinforces the hypothesis that nozzle drift is primarily governed by time, not by movement distance or pattern complexity. However, the data also shows no regularity that could be used to predict drift behavior.

One possible explanation is a sensitivity of the mechanical system to minor temperature fluctuations. Although the UPD printer is situated in an air-conditioned cleanroom environment, small thermal variations may occur due to operating equipment or the presence of personnel. At this stage, however, the cause of nozzle drift remains undetermined.

This study experimentally confirms the existence of nozzle drift in long-duration UPD print jobs. The results demonstrate that drift is primarily a time-dependent phenomenon. For short-duration print jobs, nozzle drift is unlikely to cause significant issues. For long-duration and high-precision tasks, however, incorporating a manual realignment step during printing may be necessary to maintain the desired accuracy.

3.4. Line uniformity

Depending on the application, it is often critical that printed lines exhibit high uniformity. When structures are composed of multiple segments, deviations from a uniform line are most pronounced at the segment junctions. Since conformal prints inherently consist of many short segments, particular care must be taken to ensure line homogeneity.

In this work, we evaluated three different printing strategies in terms of line uniformity: standard printing with no additional care (figure 8(a)), printing using the *veclineramp* command as discussed in section 2.1 (figure 8(b)), and a method where each line is subdivided into 5 μm -long segments (figure 8(c)). The latter method accepts that bulges at segment endpoints cannot be fully eliminated, and instead places them close enough together to create a uniformly ‘bulged’ structure.

To assess uniformity, we measured both the line width and the bulges at the connection points

between adjacent segments. Without any measures taken, i.e. using neither *veclineramp* nor segmentation, width deviations at the segment junctions reached up to 40%. This is caused by the lack of an advanced motion controller which causes the system to shortly stop between adjacent segments. Introducing the *veclineramp* command significantly reduced the width deviation to approximately 15%. This is achieved by reducing the pressure at the end of a segment which results in less excess ink being extruded during the short stop of the motion system. Segmenting the line into 5 μm intervals further improved uniformity, reducing the maximum deviation from the average line width to just 7%. The idea behind this approach is not to avoid bulges but to place them so closely that the entire line is made of them. This effectively renders them invisible.

However, the increased uniformity for segmented lines comes at the cost of an increased line width and a longer print time. To partially compensate for the wider line, the printing pressure was reduced from 9000 mbar to 6500 mbar. Nonetheless, the line width increased from 6.8 μm to 8.0 μm for a segmented line compared to one printed with no measures or with *veclineramp*.

In conclusion, we recommend using the *veclineramp* command when thinner lines and shorter printing times are prioritized. If maximal uniformity is essential, segmenting lines into 5 μm intervals is the most effective strategy. This segmentation approach may become unnecessary in future systems equipped with advanced motion controllers that allow continuous multi-segment printing without stopping between segments.

3.5. Conformal printing demonstrators

We have fabricated several demonstrators to showcase the potential of our semi-automatic conformal metal microstructure printing approach. Two different types of substrates were used for these demonstrations.

The first substrate is a glue line dispensed onto a glass slide. It has a width of 540 μm and a height of 43 μm . As a result, the slope is relatively shallow, which reduces the required alignment precision, as discussed in section 3.2. A 100 μm mesh was printed across this glue line, and a 200 μm scale bar was added next to it for reference. This demonstrator is shown in figure 9(a).

The second substrate was manufactured using μSLA printing by Horizon Microtechnologies. It features a cylindrical pyramid structure with a total height of 43 μm and near-vertical 5 μm high steps. These steep steps make precise alignment essential. To demonstrate the robustness of our approach, we printed a star-shaped pattern across the pyramid. This not only illustrates that arbitrary printing directions

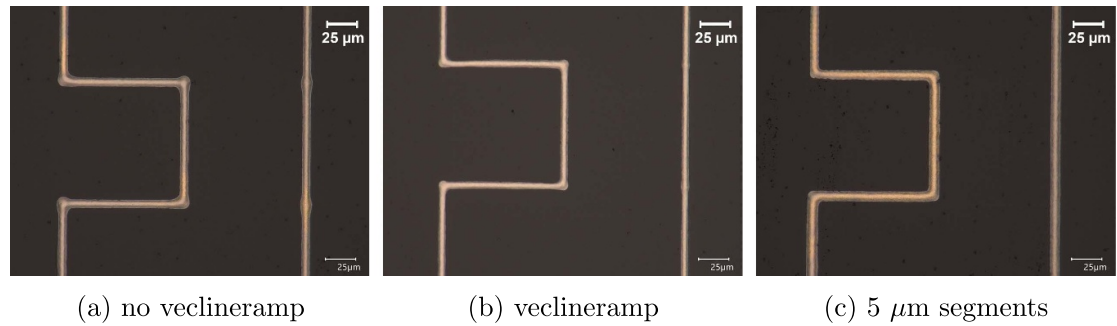
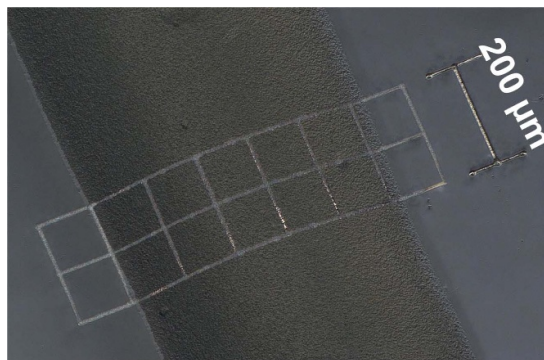
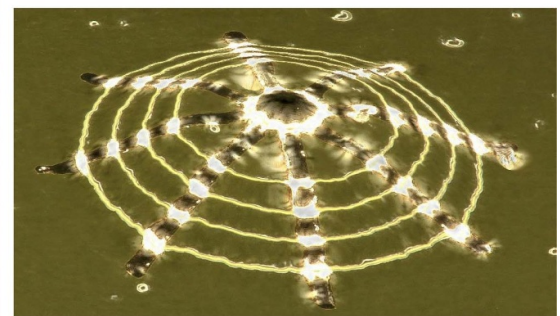


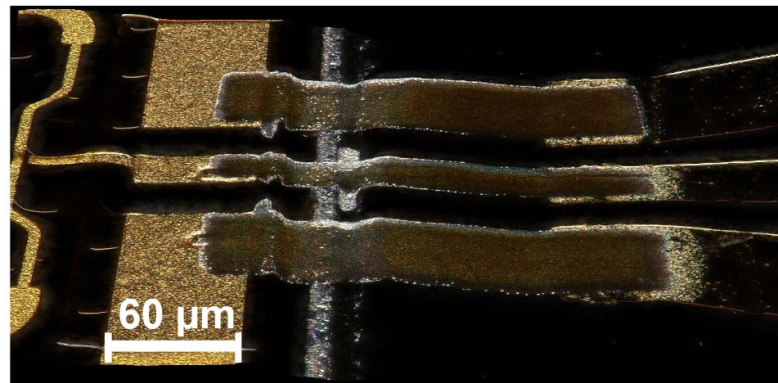
Figure 8. Printing the same structure with and without veclineramp. The Ω -shaped structure has $100\ \mu\text{m}$ long segments and the vertical line is printed with multiple $100\ \mu\text{m}$ long segments which end at the corners of the adjacent Ω -structure. The rightmost structure is printed without veclineramp but by splitting all lines in $5\ \mu\text{m}$ long segments, which also significantly increases line uniformity.



(a) Printed silver mesh over a glue line with a printed $200\ \mu\text{m}$ scalebar. The height of the glue line is $43\ \mu\text{m}$.



(b) Star printed over a circular pyramid with a height of $43\ \mu\text{m}$. The vertical steps make alignment crucial for this print.



(c) An application example: A printed radio frequency interconnect between two monolithic microwave integrated circuits on a complex surface topology as published in [28].

Figure 9. Demonstrators using the semi-automatic conformal metal microstructure printing presented in this paper.

are possible, but also highlights that the surface does not need to exhibit uniformity in any direction. Since our method is based on projecting paths onto full 3D surface measurements, it can accommodate arbitrary geometries.

We employed our semi-automatic conformal printing approach to fabricate a radio frequency

interconnect between two monolithic microwave integrated circuits with a complex surface topology. This application is illustrated in figure 9(c). The figure shows that the center conductor becomes noticeably wider after approximately one third of the total length. This is intentional behavior to compensate for changes in the dielectric properties of the material

below the interconnect and shows the excellent alignment of the printed structure. This usecase has been presented in detail in [28].

4. Conclusion

Previous approaches to conformal UPD printing have typically relied on extensive user intervention, requiring the operator to manually teach the surface geometry to the printer. The method presented in this work significantly reduces human interaction and enables conformal printing on nearly arbitrary surface topographies. Our approach is based on external surface measurement and projection of print paths onto the measured geometry, effectively eliminating the need for manual surface teaching.

We have analyzed the importance of alignment in conformal UPD printing and presented how different projection algorithms influence printing time and path segmentation. Moreover, we introduced the phenomenon of nozzle drift, and measured it in a long-term experiment. While we cannot definitely determine its cause, our experimental results indicated that nozzle drift is a time-dependent phenomenon rather than being caused by axis movement. We also discussed line homogeneity for three different printing approaches and discussed the trade-off between uniformity, printing time and line width.

In summary, this work advances the capabilities of UPD printing technology, providing a semi-automated conformal printing workflow and essential process insights to achieve the highest precision. It provides a solid foundation to make UPD printing onto non-planar surfaces an interesting option for industrial applications.

Data availability statement

All data that support the findings of this study are included within the article (and any supplementary files).

Acknowledgments

This research is supported by the Ministry of Science, Research, and the Arts of the state of Baden-Wuerttemberg, Germany, within the framework of the ‘Mobility of the Future’ Innovation Campus (ICM).

This work is supported in part by BMBF within the funding for the program Forschungslabore Mikroelektronik Deutschland (ForLab).

The authors gratefully acknowledge the Deutsche Forschungsgemeinschaft (DFG, German Research Foundation) under Germany’s Strategy via the Excellence Cluster 3D Matter Made to Order (3DMM2O, EXC-2082/1-390761711) for financial support.

Conflict of interest

The authors declare that they have no conflict of interest.

The authors declare that the findings reported in this manuscript are the result of their original research. The manuscript’s clarity and language have been enhanced with the assistance of AI-based tools, including generative AI.

Author contributions

Martin Roemhild  0000-0002-9771-7694

Conceptualization (equal), Investigation (equal), Project administration (equal), Supervision (equal), Validation (equal), Writing – review & editing (equal)

Jonathan Wendel

Software (equal), Writing – review & editing (supporting)

Lilli Weiss

Investigation (equal), Validation (equal)

Holger Baur

Methodology (equal), Project administration (equal)

Uli Lemmer

Funding acquisition (equal), Resources (equal), Writing – review & editing (supporting)

Norbert Fruehauf

Funding acquisition (equal), Project administration (supporting), Writing – review & editing (supporting)

Thomas Zwick

Funding acquisition (equal), Project administration (supporting), Writing – review & editing (supporting)

Akanksha Bhutani

Funding acquisition (equal), Project administration (supporting), Writing – review & editing (supporting)

References

- [1] Zhang S, Wang B, Jiang J, Wu K, Guo C F and Wu. Z 2019 High-fidelity conformal printing of 3D liquid alloy circuits for soft electronics *ACS Appl. Mater. Interfaces* **11** 7148–56
- [2] Roemhild M, Waldner K, Baur H and Fruehauf N 2024 Process considerations for ultraprecise deposition printing on flexible substrates *2024 IEEE Int. Flexible Electronics Technology Conf. (IFETC)* pp 1–3
- [3] Tan H W, Tran T and Chua C K 2016 A review of printed passive electronic components through fully additive manufacturing methods *Virtual Phys. Prototyping* **11** 271–88
- [4] Espera A H, Dizon J R C, Chen Q and Advincula R C 2019 3D-printing and advanced manufacturing for electronics *Prog. Additive Manuf.* **4** 245–67
- [5] Herbert R, Lim H-R, Rigo B and Yeo W-H 2022 Fully implantable wireless batteryless vascular electronics with

- printed soft sensors for multiplex sensing of hemodynamics *Sci. Adv.* **8** eabm1175
- [6] Lo Li-W, Zhao J, Wan H, Wang Y, Chakrabartty S and Wang C 2021 An inkjet-printed PEDOT:PSS-based stretchable conductor for wearable health monitoring device applications *ACS Appl. Mater. Interfaces* **13** 04
- [7] Ryoo M, Kim D, Noh J and Ahn S I 2024 3D-printed electronics for biomedical applications *Int. J. Bioprinting* **10** 4139
- [8] Khan Y, Thielens A, Muin S, Ting J, Baumbauer C and Arias A C 2020 A new frontier of printed electronics: flexible hybrid electronics *Adv. Mater.* **32** 1905279
- [9] Rose D, Ratterman M, Griffin D, Hou L, Kelley-Loughnane N, Naik R, Hagen J, Papautsky I and Heikenfeld J 2014 Adhesive RFID sensor patch for monitoring of sweat electrolytes *IEEE Trans. Bio-Med. Eng.* **62** 11
- [10] Elsobky M, Alavi G, Albrecht B, Deuble T, Harendt C, Richter H, Yu Z and Burghartz J N 2018 Ultra-thin sensor systems integrating silicon chips with on-foil passive and active components *Proceedings* **2** 748
- [11] Virtanen J, Ukkonen L, Björninen T, Elsherbeni A and Sydänheimo L 2011 Inkjet-printed humidity sensor for passive UHF RFID systems *IEEE T. Instrum. Meas.* **60** 2768–77
- [12] Zhao Y, Gao S, Zhu J, Li J, Xu H, Xu K, Cheng H and Huang X 2019 Multifunctional stretchable sensors for continuous monitoring of long-term leaf physiology and microclimate *ACS Omega* **4** 9522–30
- [13] Zymelka D, Togashi K and Kobayashi T 2020 Carbon-based printed strain sensor array for remote and automated structural health monitoring *Smart Mater. Struct.* **29** 105022
- [14] Huang Y A, Wu H, Xiao L, Duan Y, Zhu H, Bian J, Ye D and Yin Z 2019 Assembly and applications of 3D conformal electronics on curvilinear surfaces *Mater. Horiz.* **6** 642–83
- [15] Wu H, Tian Y, Luo H, Zhu H, Duan Y and Huang Y 2020 Fabrication techniques for curved electronics on arbitrary surfaces *Adv. Mater. Technol.* **5** 2000093
- [16] Adams J J, Duoss E B, Malkowski T F, Motala M J, Ahn B Y, Nuzzo R G, Bernhard J T and Lewis J A 2011 Conformal printing of electrically small antennas on three-dimensional surfaces *Adv. Mater.* **23** 1335–40
- [17] Ko H C *et al* 2008 A hemispherical electronic eye camera based on compressible silicon optoelectronics *Nature* **454** 748–53
- [18] Liu Y, Pharr M and Salvatore G A 2017 Lab-on-skin: a review of flexible and stretchable electronics for wearable health monitoring *ACS Nano* **11** 9614–35
- [19] Farooqui M F and Shamim A 2017 3-D inkjet-printed helical antenna with integrated lens *IEEE Antennas Wirel. Propag. Lett.* **16** 800–3
- [20] Mkhize N and Bhaskaran H 2022 Electrohydrodynamic jet printing: introductory concepts and considerations *Small Sci.* **2** 2100073
- [21] Optomec 2016 Aerosol jet 5X system (available at: <https://www.optomec.com/wp-content/uploads/2014/08/AJ5X-System-WEB-0216.pdf>) (Accessed 10 August 2025)
- [22] Feng J Q, Ramm A and Renn M J 2021 A quantitative analysis of overspray in Aerosol Jet® printing *Flex. Print. Electron.* **6** 045006
- [23] Lysień M *et al* 2022 High-resolution deposition of conductive and insulating materials at micrometer scale on complex substrates *Sci. Rep.* **12** 9327
- [24] XTPL Delta Printing System (available at: https://xtpl.com/wp-content/uploads/2025/03/XTPL_brochure_DPS-low.pdf) (Accessed 10 August 2025)
- [25] Roemhild M, Gramlich G, Wendel J, Baur H, Zwick T and Fruehauf N 2024 Ultraprecise printing of D-band interconnects using dielectric ramps *2024 15th German Microwave Conf. (GeMiC)* pp 57–60
- [26] Uzel S G M, Weeks R D, Eriksson M, Kokkinis D and Lewis J A 2022 Multimaterial multinozzle adaptive 3D printing of soft materials *Adv. Mater. Technol.* **7** 2101710
- [27] Ahmed R U, Dowell E, Alam C S and Rahman M S 2024 Design and development of a desktop 3D printer for conformal additive manufacturing *ASME International Mechanical Engineering Congress and Exposition* vol 88681 (American Society of Mechanical Engineers) p V010T13A020
- [28] Gramlich G *et al* 2025 Hybrid integration of a beam-steering leaky-wave antenna and power amplifier MMIC using UPD printing in 220 to 325 GHz range *IEEE Open J. Antennas Propag.* **6** 837–53